Development of an automatic routine for calibration of thermographic phosphors

Abou Nada, Fahd Jouda; Knappe, Christoph; Xu, Xin; Richter, Mattias; Aldén, Marcus

Published in:
Measurement Science & Technology

DOI:
10.1088/0957-0233/25/2/025201

2014

IOP Publishing Measurement Science and Technology
Meas. Sci. Technol. **25** (2014) 025201 (9pp) doi:10.1088/0957-0233/25/2/025201

Development of an automatic routine for calibration of thermographic phosphors

F Abou Nada, C Knappe, X Xu, M Richter and M Aldén

Department of Physics, Division of Combustion Physics, Lund University, Box 118, SE-22100, Lund, Sweden

E-mail: fahed.abou_nada@forbrf.lth.se

Received 6 May 2013, revised 1 December 2013
Accepted for publication 6 December 2013
Published 20 January 2014

Abstract

An automated routine for the continuous calibration of thermographic phosphors was developed as a replacement for the conventional calibration scheme that relied on fixed temperature points. The automated calibration routine was validated using $Mg_3F_2GeO_4$:Mn as a calibration phosphor. Hardware and software aspects of the calibration process were addressed in this development. The hardware aspect included a new substrate design using a high performance alloy, the Hastelloy-C alloy, whereas the software aspect included an automated acquisition system which was capable of acquiring simultaneous thermocouple temperatures and phosphor decay waveform in real time. The design of the calibration process eliminates the need for a system in thermal equilibrium during a phosphor calibration measurement. Temperature ramping rates of up to 4 K min^{-1} were employed in the oven without a delay in the temperature response being measured between the phosphor and the thermocouples involved. In addition, the automated calibration setup allowed for detailed investigations on the effect of heat being delivered to the phosphor coating by the laser. These findings were confirmed by a simple heat transfer model, based on lumped system analysis. In comparison to the data acquisition performed at several fixed points with the conventional calibration scheme, the experiment duration was shortened by a factor of 4 with the overall accuracy improved by 1–2 K.

Keywords: laser induced phosphorescence, calibration, thermometry, thermographic phosphors

(Some figures may appear in colour only in the online journal)

1. Introduction

Thermographic phosphors are materials for remote temperature sensing that have the capability of probing temperatures starting from cryogenic temperatures up to around 2000 K. Temperature probing applications using thermographic phosphors are extensive and include, but are not exclusive to, biological, electric, industrial and combustion research applications [1–9]. A thermographic phosphor consists of an inorganic host that is doped by an activator. The activator material can belong either to rare earth ions or transition metals [6]. Thermographic phosphors react to the change of temperature by altering their phosphorescence emission characteristics. The changing characteristics could be of a spectral or temporal nature. A spectral response for temperature changes is manifested as a wavelength shift of the emission distribution or intensity variations of spectral components, whereas a temporal response of the phosphor is detected as phosphorescence decay-time reduction with increasing temperature. Thermographic phosphor temperatures can be extracted by exploiting the different response mechanisms. Using 2D detectors, e.g. CCD or CMOS cameras, the spectral ratios of two of the phosphorescence emission lines can be employed for 2D temperature measurements [10, 11]. Similarly, by employing a detector to measure the phosphorescence decay-time, single-point and even 2D temperature measurements can be achieved [7, 12].

Measuring temperatures using thermographic phosphors requires a calibration curve for the phosphorescent material being used. The calibration curve acts as a reference that

maps the phosphorescence characteristics as a function of temperature. In this paper, the calibration of phosphorescence decay-time as a function of temperature is discussed. A well-constructed calibration curve is important for an accurate thermographic phosphor temperature determination. The process of obtaining a phosphor calibration curve can be tedious and accompanied with effects such as detector nonlinearity [13, 14]. Despite the importance of the calibration, no major development has occurred or been reported for the method by which the temperature calibration is achieved. A typical calibration curve is composed of several fixed temperature points acquired by averaging a number of decay curves at each temperature level. Measurements are usually performed with the system being in thermal equilibrium in order to avoid a potential mismatch between temperatures being measured by the thermocouples and those being measured by the phosphor. In order to obtain a calibration curve that is continuous over the entire calibrated temperature interval, subsequent data interpolation by means of smoothing polynomials can be used to fill the temperature gaps in between the data points acquired earlier. However, interpolating among calibration data points can pose a potential risk for accuracy errors, depending on deviations between the fit and the true phosphor behavior.

In this paper, the development of an automated calibration routine is described and compared to the widely used conventional calibration process. Advantages such as reduced acquisition time and higher temperature accuracy are the two improvements achieved with this routine. The aim is to continuously and simultaneously log the temperature measured by thermocouples and the associated phosphorescence decay waveform. This continuous acquisition runs while the phosphor was heated at a constant rate of 1.6 K min^{-1}, hence, the oven did not stabilize at predefined temperatures. To evaluate the developed calibration scheme, manganese-doped magnesium fluorogermanate ($Mg_3F_2GeO_4$:Mn) [15] was chosen. This phosphor is sensitive over a wide temperature range, its decay-time extending from around 3 ms at 290 K to around 50 ns at 1100 K [16]. $Mg_3F_2GeO_4$:Mn was efficiently excited using pulsed UV laser radiation at 355 nm. The corresponding emission spectrum is composed of multiple peaks within a spectral range of 600–700 nm, the strongest emission peak being centered at 659 nm, see figure 1. Phosphorescence was detected at a central wavelength of 656 nm using an interference filter with a full width half maximum (FWHM) of 10 nm. $Mg_3F_2GeO_4$:Mn exhibits a quasi-single exponential decay form, as shown by the example decay in figure 2. A test conducted earlier by the authors showed that the limited bit resolution has an insignificant effect on the error of the evaluated decay-time.

A single-exponential relation, provided by equation (1), is used to describe the exponential decay of $Mg_3F_2GeO_4$:Mn phosphorescence, where $I(t)$ and I_0 are the intensity of the decay at any given time t and at $t = 0$, respectively. τ is associated with the decay-time and C is a constant signal offset

$$I(t) = I_0 \, e^{-t/\tau} + C. \quad (1)$$

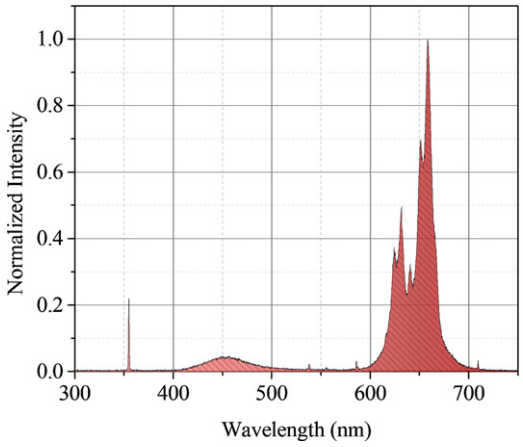

Figure 1. $Mg_3F_2GeO_4$:Mn emission spectrum with laser excitation at 355 nm.

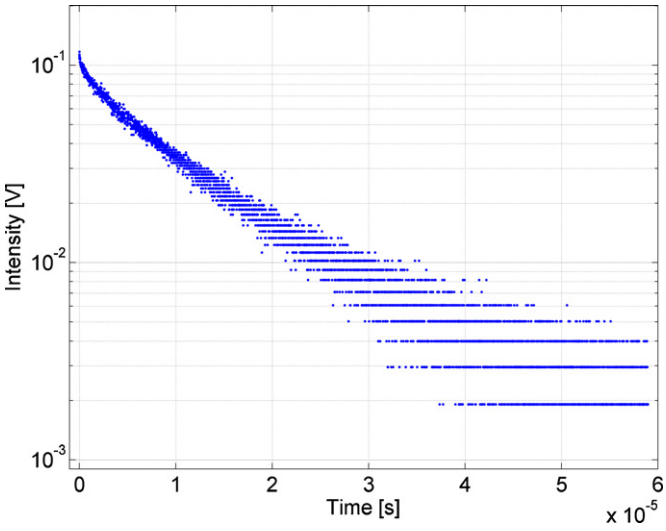

Figure 2. $Mg_3F_2GeO_4$:Mn phosphorescence decay curve at a temperature of 840.6 K. The horizontal gaps between single data points are a result of limited bit resolution in the oscilloscope's data acquisition software.

2. Experimental setup

The basic components of the experimental setup are shown in figure 3. To excite $Mg_3F_2GeO_4$:Mn, a pulsed Nd:YAG laser was used, operating at 10 Hz and having a pulse duration of 6 ns at FWHM. $Mg_3F_2GeO_4$:Mn was effectively excited in the UV spectral region using the third harmonic of a Nd:YAG laser operating at 355 nm. Unfocused laser pulses excited a phosphor layer that was coated on Hastelloy-C alloy substrate. The laser beam is of circular profile and had a diameter of 12 mm and pulse energy of 10 mJ, this resulting in a laser energy density of 8.8×10^{-3} J cm^{-2}.

Several in-house developed temperature calibration substrates were manufactured. The substrates were made of discs of Hastelloy-C alloy. Hastelloy-C alloy is a highly corrosion-resistant material with a relatively low expansion coefficient, which minimizes the risk of the phosphor coating flaking off due to thermal expansion of the disc. Its high melting temperature (above 1550 K) makes Hastelloy-C a

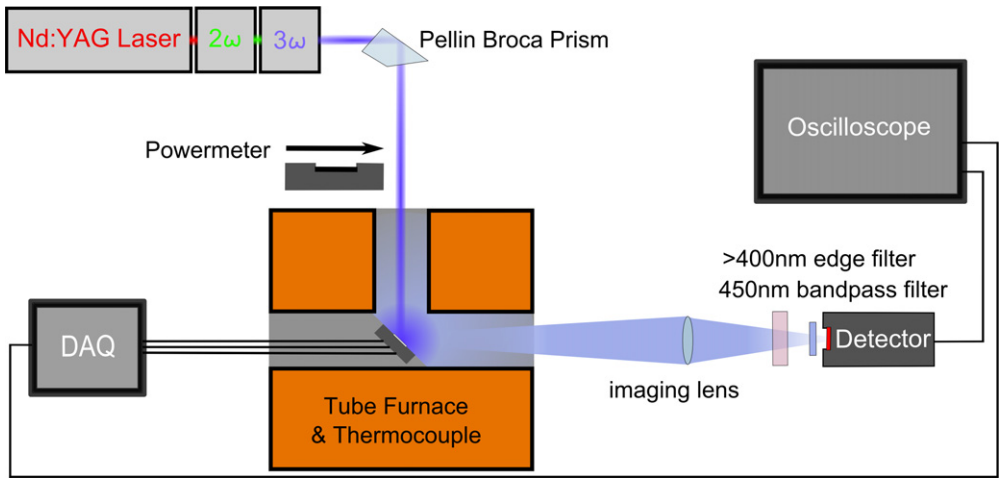

Figure 3. Experimental setup for the automated temperature calibration of a thermographic phosphor. Both the temperature logging and the phosphorescence detection are synchronized to realize simultaneous temperature-decay-time measurements.

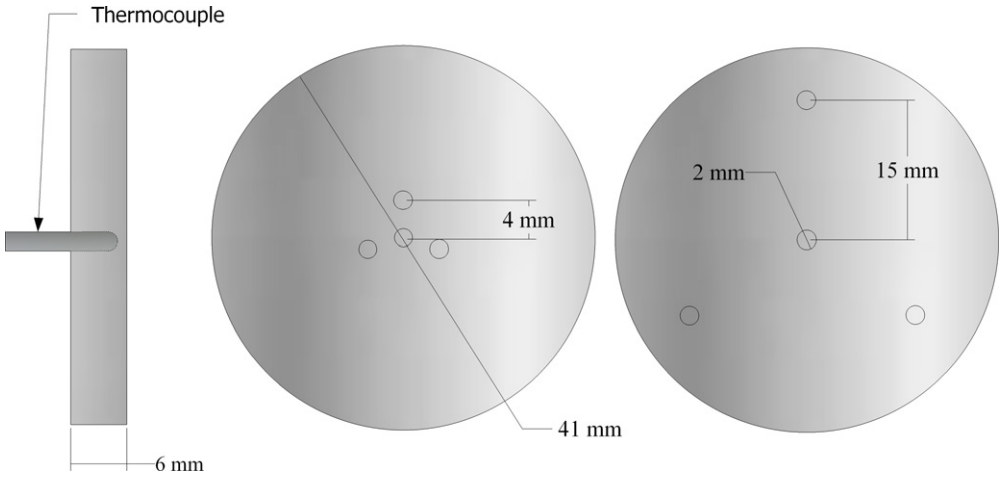

Figure 4. Hastelloy-C calibration substrate plate design.

suitable substrate material for the majority of thermographic phosphors. The design of the Hastelloy-C calibration discs is shown in figure 4. Each substrate was equipped with four type-K thermocouples. The thermocouples used are insulated by densely packed magnesium oxide and sheathed with an Inconel 600 alloy tube of 2 mm in diameter. The thermocouples were placed deep in the back of the substrate providing minimum separation to the coated surface. For accurate point measurement calibrations, thermocouples were positioned in a cluster close to the center of the substrate, whereas for probing temperature gradients across the substrate surface, thermocouples can be arranged in a more spread-out configuration. The Inconel sheaths of the thermocouples allowed the substrate to be suspended in the furnace without touching the furnace ceramic walls. The suspension of the substrate prevents the occurrence of thermal gradients that could be caused by a local increase in the heat transfer due to wall–substrate conduction. An oven of T-junction design (see figure 3) with a maximum operating temperature of 1500 K was used to generate different temperatures for the calibration procedure. Quartz windows were installed at the front and side ports of the oven to increase the thermal stability by reducing convective flows through the oven tubes.

Phosphorescence emission was collected and focused onto the detector window by a plano-convex lens with a focal length of 300 mm. A Hamamatsu H11526–20-NF photomultiplier tube was used as the detector. According to recent investigations by the authors, this PMT type showed superior signal linearity compared to other detector types [13]. A control voltage of 0.339 V set the photomultiplier gain constant throughout the entire experiment. The phosphorescence was spectrally narrowed by the use of an interference filter centered at 656 nm with FWHM of 10 nm. To further suppress any scattered laser radiation, a long pass filter with a cutoff wavelength at 400 nm was mounted in front of the interference filter. The PMT output was connected via a BNC cable to the oscilloscope terminal with a 50 Ω termination resistance. A data acquisition system with a LabVIEW interface was used to log temperatures from the four thermocouples and synchronize them with decay signals, measured by the oscilloscope. The program design was focused on the automated and simultaneous acquisition and processing of data needed to build a calibration curve for

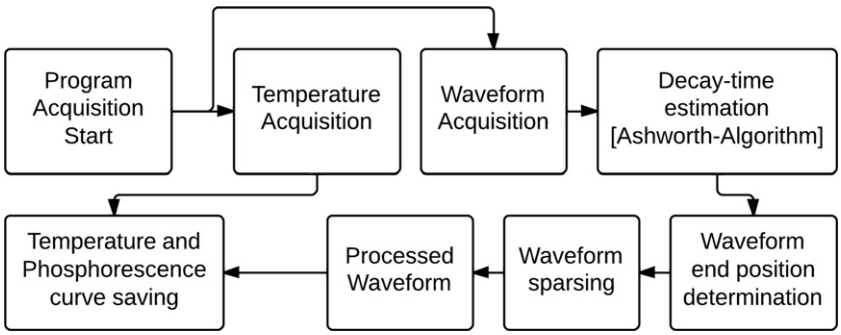

Figure 5. Program flowchart, for automated temperature calibration.

any selected phosphor. A flowchart illustrating the program design can be found in figure 5.

During a calibration, both the decay-time and the emission signal strength vary with temperature as it increases. This requires the calibration routine to have the capability to adapt to these changes by adjusting the base-time and voltage gain of the oscilloscope. The most suitable oscilloscope settings are automatically calculated and implemented. Desired initial settings for time-base and voltage range can be set manually by the user prior to the calibration experiment. The automation process uses the decay-time and peak intensity of the latest acquired waveforms as input values for determining the suitable settings for the following waveform acquisition. The voltage range was computed by averaging the peak intensities of the last five acquired waveforms. To account for pulse-to-pulse variation, a value of 20% of the averaged peak intensities was added as a margin to the *y*-axis scale of the oscilloscope, making sure that the phosphorescence peak is always contained in the acquired signal. This process is straightforward in contrast to the time-base resolution calculation method, which requires a fast and reliable decay-time estimate of the recorded phosphorescence decay waveform.

For this purpose, Ashworth's rapid lifetime determination (RLD) algorithm [17–21] was implemented. The RLD algorithm is estimated to perform three orders of magnitude faster than the weighted nonlinear least squares method [19]. Under the same noise levels, the RLD algorithm has a precision comparable to that of the weighted nonlinear least squares method. The decay-time calculated in real time with the RLD algorithm from a curve being acquired was used to set the time resolution of the oscilloscope. Also, the RLD-computed decay-time was implemented by the waveform processing section of the program to define the end of the decay curve, which was set to five decay-times starting after the peak of the exponential decay of the phosphorescence signal.

Sampling 250 k data points per curve is necessary for a proper time resolution of the phosphorescence peak, but at the same time weighs heavily in the size of the file when the waveform has to be saved for further post-acquisition analysis. An adequate solution for file size reduction is the employment of variable sparsing of the decay-signal waveforms; which means saving only every *n*th data point from an acquired waveform. To warrant a high resolution of the phosphorescence signal peak, selective sparsing was

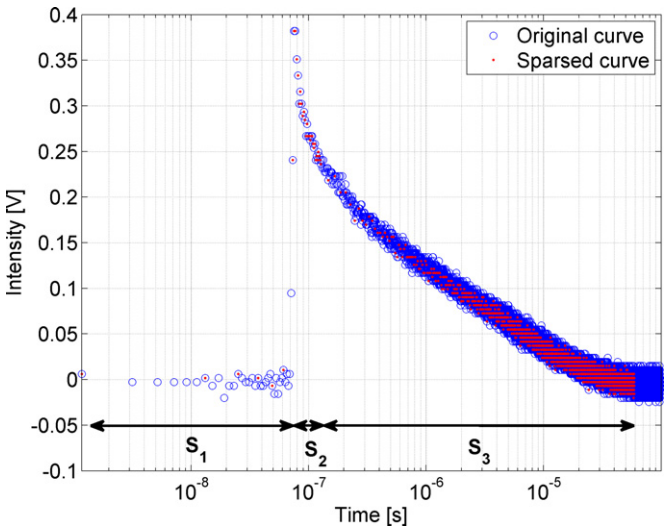

Figure 6. Selectively sparsed and original phosphorescence decay curve. The number of data points in each segment is given as follows: S_1 200 data points, S_2 original number of data points and S_3 3000 data points with 50 k data points as the original number of points

chosen which preserves the accurate peak position. In selective sparsing, the decay curve is divided into three sections, the first section comprises the constant signal prior to the signal peak, the second extends from the peak to a cutoff point set at 10 ns after the signal peak and the third section includes the residual part of the curve. Sparsing factors S_i for each section i can be varied individually, depending on the number of data points desired in each of the sections. For this study, S_1 was set to 300 data points, S_2 was set to the original number of data points and S_3, i.e. the temperature-sensitive part of the decay, was set to contain 4000 data points. In case the number of data points in any segment is below the assigned value, the original number of data points is kept and no sparsing occurs. The main advantage of selective sparsing lies in the reduction of unnecessary information whilst preserving necessary curve features, needed for achieving results with satisfactory precision. An example of selective sparsing of a phosphor decay curve is displayed in figure 6. In order to visually enhance the effects of sparsing on a curve, different sparsing settings were used to produce figure 6 compared to those which were used in the experiment. Assuming the sparsing settings used in the experiment to reduce the original

waveform length of 250 k points, the file size of the data saved in LabVIEW's default tdms file format was decreased by a factor of approximately 55 in relation to the original file size.

After this waveform processing, both temperature data and phosphorescence signals are saved within the same file, which allows the matching of each waveform and its corresponding decay-time with a temperature that was measured simultaneously. Upon completion of a temperature calibration measurement, the files containing the temperature value and phosphorescence waveform were evaluated in order to generate a phosphor-specific calibration curve. Temperatures were calculated from the mean value of the four simultaneously achieved thermocouple temperatures. Phosphorescence decay curves were processed according to pre-fitting conditions set globally for all of the curves. Those fitting conditions essentially define global criteria for the evaluation window, which are applied for each curve. Thus, the beginning of each fitting window is set to a constant time value of 10 ns after the phosphorescence peak. The fitting window end, in contrast, is determined as the time when the curve has reached 9% of the initial peak value which is roughly around 2.5 decay-times after the start of the decay. After determining the fitting window for each curve, the segment of the curve that is meant to be fitted is passed on to the least-squares fitting algorithm. A baseline correction was applied by subtracting the mean of the constant signal prior to the peak from the entire curve thus reducing the number of fitted parameters to 2 instead of 3.

The RLD algorithm provides a fast and relatively accurate estimation of the phosphorescence decay-time during the calibration acquisition. The RLD estimated decay-time was later used by the routine to set the controls for the following waveform acquisition. After the entire phosphor calibration acquisition is done, a nonlinear least square algorithm (NLLS) is used to provide more accurate decay-times. The NLLS is orders of magnitude slower than the RLD algorithm, so the NLLS is only implemented for decay-time evaluation that is finally used to build the calibration curve. Thus, the RLD algorithm functionality is limited to the online control of the automated calibration routine.

3. Results and discussion

An automated temperature calibration of $Mg_3F_2GeO_4$:Mn was realized and compared to a conventional calibration in order to establish a comparison in terms of measurement accuracy and experiment time. A plot showing both automatic and conventional calibration results is shown in figure 7.

The two calibrations were carried out within a temperature range starting around 290 K and ending around 1070 K. Both calibrations were conducted under similar experimental conditions, i.e. laser energy density and detector gain. The conventional calibration was produced by taking measurements at temperature intervals of around 50 K. After reaching thermal equilibrium, 100 phosphorescence decay curves are saved and processed to obtain 100 decay-times and their corresponding temperatures which are then averaged to obtain a single data point. This procedure is repeated

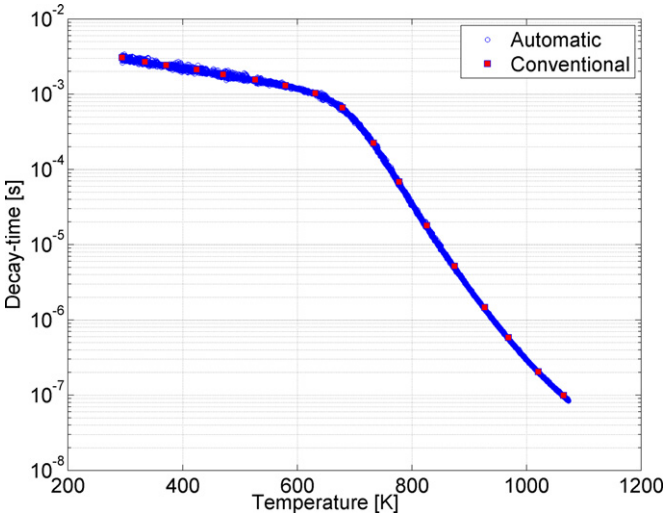

Figure 7. Automatic and conventional calibration curves for $Mg_3F_2GeO_4$:Mn.

at every chosen calibration temperature. However, during automatic calibration, the oven was ramped up continuously at a constant heating rate of 1.6 K min^{-1} while acquiring phosphorescence decay curves at a rate of 1 waveform per second. These acquisition settings resulted in an average temperature separation of 0.027° between two consecutive curves.

The speed at which the automated calibration curve can be run by is limited by the maximum heating rate of the oven and the acquisition rate of the system. A maximum heating rate of 4 K min^{-1} and an acquisition rate of 1 acquisition per second for 800 K temperature range result in a calibration duration of at least 3.4 h with an average temperature separation of 0.07 K. The automatic calibration of $Mg_3F_2GeO_4$:Mn required little more than 8 h, bearing in mind that the oven was set to a heating rate of around 1.6 K min^{-1}. In comparison, the conventional calibration, with only 17 averaged measurement points, required almost 32 h to complete (including a 12 h break during the night). The prolongation is due to the requirement of establishing thermal equilibrium in the conventional calibration. Reaching thermal equilibrium takes more time at lower temperatures, where heat losses to the surrounding occur at a slower rate. The automated calibration achieved a reduction of the experiment duration by a factor of 4 compared to the conventional calibration. This improvement in calibration duration could be further improved by setting the heating rate of the oven to a higher value.

To study the accuracy of the developed calibration procedure, the two calibration curves were subjected to a smoothing spline polynomial that relates the temperature to the natural logarithm of the decay-time. The benefit of the smoothing spline polynomial was evaluated by comparing the distribution of residuals around the zero line of the fitting polynomial. A fit is considered to be of good quality if the residuals are distributed symmetrically around the zero line. Two polynomials were obtained, one for each calibration curve. In order to compare the two obtained polynomials in terms of accuracy, an array of generated decay-times starting

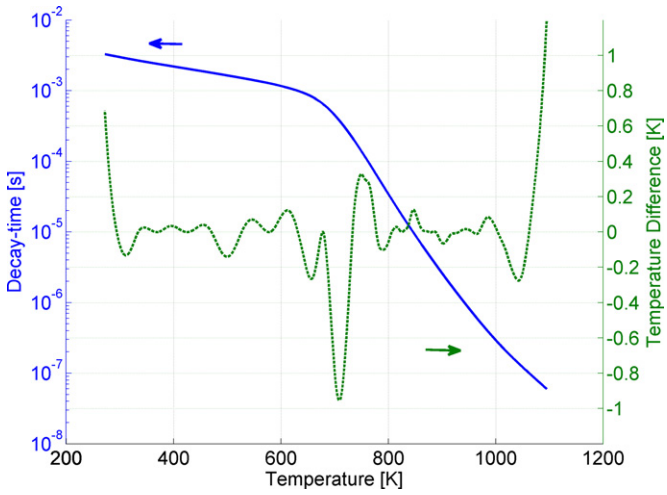

Figure 8. Comparison of conventional and automatic calibration polynomials by temperature difference analysis. A $Mg_3F_2GeO_4$:Mn calibration curve (solid-blue, left *y*-axis) and the temperature difference between the two calibration polynomials (dotted-green, right *y*-axis) are displayed.

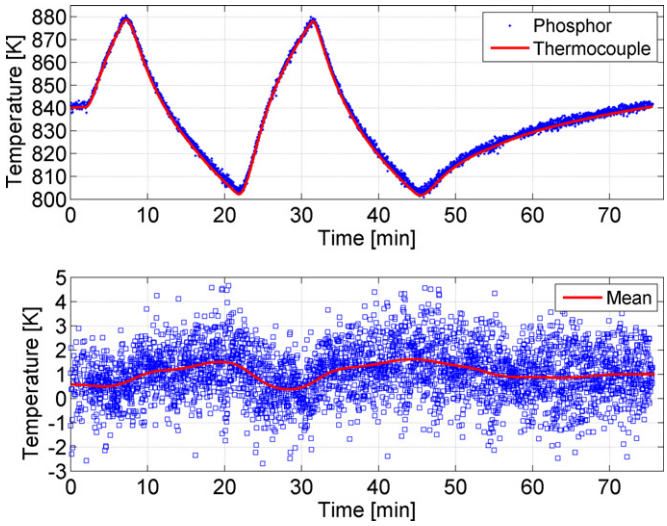

Figure 9. (Top)—phosphor response plot to an induced temperature oscillation. (Bottom)—temperature difference between evaluated phosphor temperature and average thermocouple temperature along with the corresponding smoothing average.

from a decay-time of 3.3 ms down to 60 ns was created. The natural logarithm of the generated decay-times was inserted into the automatic calibration polynomial, giving a simulated temperature. Then by using this generated temperature array, decay-times that correspond to the conventional calibration temperatures are found. A fitting polynomial was applied to the conventional calibration data and a temperature array was calculated from the fitting polynomial. The difference between the two temperature arrays was plotted against temperature along the generated automatic calibration curve, see figure 8.

Figure 8 shows that at the beginning of the calibration the temperature difference between the two polynomials is almost 0.7 K. The most noticeable temperature difference is located at 710 K. This point marks the beginning of an increasing sensitivity of the phosphor due to the higher temperature dependence of the phosphor quenching rates. At this turning point, the automated calibration provided a better description of the phosphor's response due to a much higher data point density in the calibration curve. Also, the temperatures derived from the conventional and automatic fitting polynomials deviate from each other mostly at the extremes of the temperature range due to the failure of the polynomials to extrapolate out of the temperature range accurately. Even though the difference in temperature in the phosphor range of interest is small, it still shows that the automatic calibration introduces improved accuracy compared to the conventional calibration method. This improvement in accuracy can be attributed to the high number of data points in the calibration curve achieved with the automated measurement routine, which allows the calibration polynomial to accurately describe the behavior of the chosen phosphor with temperature throughout the entire temperature range that was measured.

Acquiring calibration data while continuously ramping the oven temperature meant that thermal equilibrium is not met and only quasi-thermal equilibrium is achieved. Thus, it is critical to check whether the thermocouples are responding without any delay being introduced between the registered thermocouple temperatures and the phosphor coating temperature. To test this aspect, temperature oscillations were generated in the range between 805 and 880 K creating a wide range of heating rates while heating and cooling the phosphor. Figure 9 represents the thermocouple temperature profile along with the evaluated phosphor temperature. The difference between the two measured temperatures is provided in a sub-plot. Three heating and two cooling cycles were applied to provide measurement replicas. The phosphor and the thermocouple temperatures match very well, giving an indication that the thermocouples respond quickly to the phosphor coating temperature changes.

To further confirm the absence of thermocouple response delay, the heating rates of the averaged thermocouple temperatures were plotted against the corresponding phosphor heating rates (see figure 10). Heating rates extending over a range of ± 10 K min^{-1} were achieved. This range spreads well beyond the maximum heating rate of 4 K min^{-1} which was specified by the oven manufacturer for safe operation. The heating rate of the averaged thermocouple temperature agrees well with the phosphor's heating rate. A linear fit with a slope of nearly 1 and an offset constant of about 0 confirms the previous conclusion that the response of the thermocouples is quick enough to track the temperature changes experienced by the phosphor coating.

One possible application of the automated calibration setup is the measurement of heat transferred optically to the phosphor sample by the laser. Figure 11 shows temperature development of the phosphor sample over time, measured by the center thermocouple. While the surrounding environment was kept at room temperature ($T = 294$ K), the sample was exposed to 10 Hz pulses of three different laser energies: 1 mJ (thin line), 5 mJ (middle line) and 12 mJ (thick line). Corresponding dashed lines represent the lumped system analysis model. The black dotted line indicates the temperature

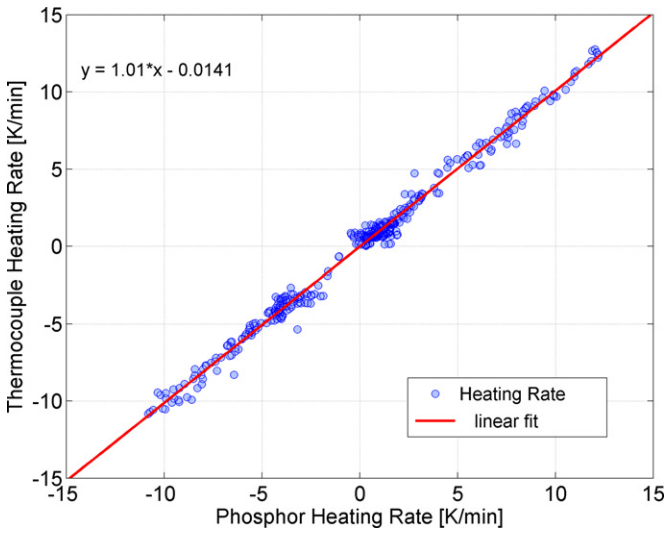

Figure 10. Cooling and heating rates of averaged thermocouple temperatures versus the corresponding phosphor coating heating rates.

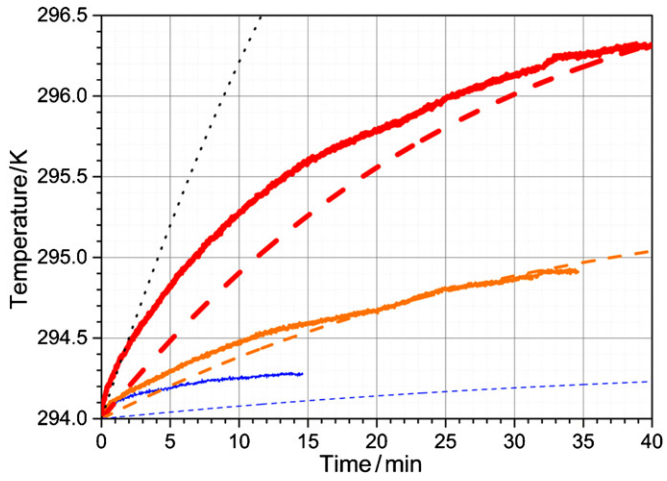

Figure 11. Comparison of measurement (lines) and model (dashed lines) on the effect of laser-induced heating of the calibration target. Three different laser energies were chosen: 1 mJ (thin blue line), 5 mJ (orange line) and 12 mJ (thick red line). The dotted line corresponds to a black body, heated with 12 mJ.

increase of a corresponding black body with $R = 0$ and $q = 0$, exposed to a laser energy of 12 mJ.

In the following, a few more details on the model are given: the model acts on the assumption that 20% of the laser energy gets reflected by the white phosphor-coated surface. This value is close to the reflectivity of YSZ TBC coatings, reported in [22], which was approximated by known values for UV absorption in TBC spray coatings. In addition, it was assumed that the residual laser energy transforms $100 \cdot (1 - q)\%$ into heating the phosphor target, assuming a phosphorescence quantum yield of $q = 0.5$, which is typical for lamp phosphors [23]. The phosphorescence quantum yield q describes the fraction of absorbed photons at wavelength λ_1 that results in the emission of a phosphorescence photon at $\lambda_2 > \lambda_1$. In terms of mass, the existence of a few micrometer thick phosphor film [24] was neglected in comparison to the much larger substrate mass.

The average temperature increase ΔT_+ per laser pulse with an energy E can then be calculated according to equation (2)

$$\Delta T_+ = (1 - R) \cdot (1 - (\lambda_1/\lambda_2)q) \cdot E/(c_v \cdot \rho \cdot \pi r^2 h). \quad (2)$$

In equation (2), ρ denotes the density, c_v the specific heat, r the radius and h the thickness of the Hastelloy substrate disc. For the highest laser energy in the test, this corresponds to $\Delta T = 171$ μK per laser pulse. After the first laser pulse, the target is no longer in thermal equilibrium with the ambient air and transfers heat energy to the surroundings. The amount of heat, that is lost per time interval dt corresponds to a decrease in temperature ΔT_- and is dependent on the actual temperature difference ΔT between the sample and the surrounding air. ΔT_- was calculated using equation (3)

$$\Delta T_- = \alpha \cdot 2\,(h + r) \cdot \Delta T \cdot \mathrm{d}t/\,(c_v \cdot \rho \cdot r \cdot h)\,. \quad (3)$$

The parameter α hereby denotes the heat transfer constant and comprises contributions from heat transfer through natural convection and radiation. It was calculated according to equation (4)

$$\alpha = \frac{0.68072 \cdot \lambda}{\left[1 + (2Pr)^{-\frac{9}{16}}\right]^{\frac{4}{9}}} \cdot \left\{\frac{Pr\, g\beta\Delta T}{[2\pi r(r+h)]^{\frac{1}{2}} \cdot \upsilon^2}\right\}^{\frac{1}{4}} + \varepsilon \cdot \sigma \cdot (2T_r + \Delta T) \cdot \left[(\Delta T + T_r)^2 + T_r^2\right]. \quad (4)$$

In equation (4), g denotes the gravitational constant, σ the Stefan–Boltzmann constant, ε the emissivity of the substrate, T_r is the ambient air temperature, λ the thermal conductivity of air, β the volumetric thermal expansion coefficient of air, υ the kinematic viscosity of air and Pr the Prandtl number of air. Further details on the assumptions for α and the lumped system analysis can be found in the appendix.

The modeled temperatures in figure 11 agree fairly well with the measured values, considering the amount of necessary assumptions. Generally, there is a trend in the model to act slower than the measured values would suggest. This stands out especially when comparing the agreement of the model to the 1 mJ laser energy measurement. The model of the black body exposed to 12 mJ expresses an upper limit of heat transfer to the sample. Around $t = 0$, also $\Delta T \approx 0$ applies and also the heat transfer to air approaches zero, see equation (3). However, the corresponding measured data (red thick line) still exhibit a higher heating rate in comparison. This behavior may have been caused by local temperature gradients across the substrate due to slow conduction. Since the thermocouple measured the temperatures very close to the laser illumination area, local heating rates might be higher than the lumped system analysis projected across the entire body.

4. Conclusions

An automated system for achieving fast and continuous temperature calibrations of thermographic phosphors is described in this paper and compared to a discrete calibration approach using $Mg_3F_2GeO_4$:Mn. The broad temperature and decay-time range of $Mg_3F_2GeO_4$:Mn was deemed

suitable for evaluating the capabilities of the presented calibration approach. A phosphor substrate made from high-performance alloy embedded with four thermocouples was designed with a concern towards phosphor and thermocouple temperature gradient minimization. Ashworth's rapid lifetime determination algorithm was applied by the acquisition software to estimate the length of each waveform being saved during the data acquisition.

The automation of the phosphor calibration process yielded an improvement in the accuracy of the obtained calibration curve and shortened the experiment duration significantly. A temperature range of 100 K could be covered in 25 min, if the maximum heating rate of the oven was applied. A high data point density of several measurements per Kelvin, as achieved by the automated calibration procedure, provided a better description of the response of phosphor decay-time to temperature and hence resulted in improvements of the temperature accuracy by about 1 K as compared to a corresponding fixed-point calibration. In addition, the automated calibration setup was used to measure the effect of laser-induced heating with a high temporal resolution, which allowed for verification of a crude heat transfer model for estimating the temperature offset, introduced by the excitation source.

Acknowledgment

The research leading to these results has received funding from the European Union Seventh Framework Programme (FP7/2007-2011) under grant agreement no. 265861 (Helios).

Appendix. Lumped system analysis

A perquisite for using the lumped system analysis approximation is the evaluation of the Biot number *Bi*, which describes the ratio between conduction and convection rates. If $Bi < 0.1$, temperature gradients across the solid material stay well within 5% [25]. The Biot number *Bi* describing this system is given by equation (A.1):

$$Bi = \frac{\alpha_{\text{conv}} \cdot r}{\lambda_h}. \tag{A.1}$$

Coefficients for convective heat transfer in gases vary from 2 to 25 W m^{-2} K^{-1} [26]. Thermal conductivity of Hastelloy at room temperature was found to be $\lambda_h = 10.1$ W m^{-1} K^{-1}. These values, together with the sample radius *r*, yield a Biot number in between 0.004 and 0.051 and legitimize the lumped system analysis assumption.

The actual heat transfer coefficient for natural convection (first summand in equation (4)) was estimated as follows according to empirical models, summarized in [27]. It can be described using the Nusselt number *Nu* using equation (A.2)

$$\alpha_{\text{conv}} = \frac{\lambda}{L} Nu. \tag{A.2}$$

The variable *L* in (A.2) denotes the characteristic length of the body. It was chosen to be the square root of the body surface as described in equation (A.3)

$$L = \sqrt{A_{\text{cyl}}} = \sqrt{2\pi r\,(r+h)}. \tag{A.3}$$

The Nusselt number for natural convection is defined by the Prandtl number *Pr*, the body-gravity function $G_L = 1.016$ (for a flat cylinder disc with horizontal axis and *L* according to (A.3)) and the Rayleigh number *Ra* for natural convection in equation (A.4)

$$Nu = \frac{0.670}{\left[1 + (2Pr)^{-\frac{9}{16}}\right]^{\frac{4}{9}}} \cdot G_L \cdot Ra^{\frac{1}{4}}. \tag{A.4}$$

The Prandtl number of air was estimated to be $Pr = 0.713 = \text{const}$ at room temperature due to the expectation that ΔT remains small. The Rayleigh number *Ra* is similar to the Reynolds number in corresponding forced convection scenarios and is defined as given by equation (A.5)

$$Ra = Pr \cdot \frac{g\beta \Delta T L^3}{v^2}. \tag{A.5}$$

Tabular values for air parameters were used, such that $\beta = 0.00343$ K^{-1} and $v = 15.11 \times 10^{-6}$ m^2 s^{-1}. Combining equations (A.2)–(A.5), finally yields the convective heat transfer coefficient, given in equation (4). For a maximum temperature increase of $\Delta T = 5$ K, α_{conv} yields a maximum value of 4.1354 W m^{-2} K^{-1}. This again is within the expected range for convective gases and results in a better estimate for the Biot number of 0.008, which again justifies the estimation of a lumped capacity model.

References

[1] Allison S W and Gillies G T 1997 Remote thermometry with thermographic phosphors: instrumentation and applications *Rev. Sci. Instrum.* **68** 2615–50

[2] Aldén M, Omrane A, Richter M and Särner G 2011 Thermographic phosphors for thermometry: a survey of combustion applications *Prog. Energy Combust. Sci.* **37** 422–61

[3] Brübach J, Pflitsch C, Dreizler A and Atakan B 2013 On surface temperature measurements with thermographic phosphors: a review *Prog. Energy Combust. Sci.* **39** 37–60

[4] Feist J P, Heyes A L and Seefeldt S 2002 Thermographic phosphors for gas turbines: instrumentation development and measurement uncertainties *11th Int. Symp. on Application of Laser Techniques to Fluid Mechanics (Lisbon, Portugal, 2002)*

[5] Allison S W and Gillies G T 2010 Fluorescence excitation and propagation through brain phantom gelatins: measurements and potential applications *Meas. Sci. Technol.* **21** 085802

[6] Khalid A and Kontis K 2008 Thermographic phosphors for high temperature measurements: principles, current state of the art and recent applications *Sensors* **8** 5673–744

[7] Someya S, Uchida M, Tominaga K, Terunuma H, Li Y and Okamoto K 2011 Lifetime-based phosphor thermometry of an optical engine using a high-speed CMOS camera *Int. J. Heat Mass Transfer* **54** 3927–32

[8] Fuhrmann N, Baum E, Brubach J and Dreizler A 2011 High-speed phosphor thermometry *Rev. Sci. Instrum.* **82** 104903

[9] Salem M, Staude S, Bergmann U and Atakan B 2010 Heat flux measurements in stagnation point methane/air flames with thermographic phosphors *Exp. Fluids* **49** 797–807

[10] Omrane A, Särner G and Aldén M 2004 2D-temperature imaging of single droplets and sprays using thermographic phosphors *Appl. Phys.* B **79** 431–4

[11] Heyes A L, Seefeldt S and Feist J P Two-colour phosphor thermometry for surface temperature measurement *Opt. Laser Technol.* **38** 257–65

[12] Euler M, Kissel T, Dreizler A and Brübach J 2011 The spectrally resolved luminescence decay of thermographic phosphors *Meas. Sci. Technol.* **22** 083001
[13] Knappe C, Nada F A, Richter M and Alden M 2012 Comparison of photo detectors and operating conditions for decay time determination in phosphor thermometry *Rev. Sci. Instrum.* **83** 094901
[14] Knappe C, Linden J, Nada F A, Richter M and Alden M 2012 Investigation and compensation of the nonlinear response in photomultiplier tubes for quantitative single-shot measurements *Rev. Sci. Instrum.* **83** 034901
[15] Brübach J, Feist J P and Dreizler A 2008 Characterization of manganese-activated magnesium fluorogermanate with regards to thermographic phosphor thermometry *Meas. Sci. Technol.* **19** 025602
[16] Brübach J, Zetterberg J, Omrane A, Li Z S, Aldén M and Dreizler A 2006 Determination of surface normal temperature gradients using thermographic phosphors and filtered Rayleigh scattering *Appl. Phys.* B **84** 537–41
[17] Woods R J, Scypinski S and Love L J C 1984 Transient digitizer for the determination of microsecond luminescence lifetimes *Anal. Chem.* **56** 1395–400
[18] Ballew R M and Demas J N 1989 An error analysis of the rapid lifetime determination method for the evaluation of single exponential decays *Anal. Chem.* **61** 30–33
[19] Ballew R M and Demas J N 1991 Error analysis of the rapid lifetime determination method for single exponential decays with a non-zero baseline *Anal. Chim. Acta* **245** 121–7
[20] Waters P D and Burns D H 1993 Optimized gated detection for lifetime measurement over a wide range of single exponential decays *Appl. Spectrosc.* **47** 111–5
[21] Moore C, Chan S P, Demas J N and DeGraff B A 2004 Comparison of methods for rapid evaluation of lifetimes of exponential decays *Appl. Spectrosc.* **58** 603–7
[22] Liu D, Lord O, Stevens O and Flewitt P E J 2013 The role of beam dispersion in Raman and photo-stimulated luminescence piezo-spectroscopy of yttria-stabilized zirconia in multi-layered coatings *Acta Mater.* **61** 12–21
[23] Feist J P and Heyes A L 2009 Photo-stimulated phosphorescence for thermal condition monitoring and nondestructive evaluation in thermal barrier coatings *Heat Transfer Eng.* **30** 1087–95
[24] Knappe C, Algotsson M, Andersson P, Richter M, Tunér M, Johansson B and Aldén M 2013 Thickness dependent variations in surface phosphor thermometry during transient combustion in an HCCI engine *Combust. Flame* **160** 1466–75
[25] Çengel Y A 2006 *Heat and Mass Transfer: A Practical Approach, SI Version* (New York: McGraw-Hill Education)
[26] Incropera F P 2007 *Fundamentals of Heat and Mass Transfer* 6th edn (Hoboken, NJ: Wiley)
[27] Lee S, Yovanovich M M and Jafarpur K 1991 Effects of geometry and orientation on laminar natural convection from isothermal bodies *J. Thermophys. Heat Transfer* **5** 208–16